Assessment Report on Innovative Rotor Blades (MAREWINT WP1,D1.3)

McGugan, Malcolm; Leble, Vladimir ; Pereira, Gilmar Ferreira

Publication date:
2015

Document Version
Publisher's PDF, also known as Version of record

Assessment Report on Innovative Rotor Blades (Marewint WP1, D1.3)

DTU Vindenergi
E Rapport 2015

Malcolm McGugan, Vladimir Leble and Gilmar Pereira

DTU Wind Energy E-0096

November 2015

MARE-WINT
new MAterials and REliability in offshore WINd Turbines technology

DTU Vindenergi
Institut for Vindenergi

Authors: Malcolm McGugan, Vladimir Leble and Gilmar Pereira
Title: Assessment Report on Innovative Rotor Blades (Marewint WP1, D1.3)
Institute: DTU Wind Energy

DTU Wind Energy E-0096

Summary:

The offshore wind energy industry faces many challenges in the short to medium term if it is to meet the ambitions of the global community for sustainable energy supply in the future. Not least among these challenges is the issue of rotor blades. Innovative design for “smart” rotor blades with embedded sensors and actuation are being developed that will deliver an improved whole-life performance, and a structural health management based operational concept.

In this report, the work of two early stage researchers within the Initial Training Network MAREWINT is presented that support the innovative concept development for wind turbine blades. This covers models and experiments with damage measurement systems embedded within the composite material/structure and numerical methods investigating the effects of leading and trailing edge flaps on modifying the aerodynamic loads on the operating rotor.

Kontrakt nr.:
MARE-WINT 309395

Projektnr.:
43155 X-1

Sponsorship:
FP7-PEOPLE-2012-ITN

ISBN:
978-87-93278-52-3

Pages: 41
Tables: 4
Figures: 26
References: 24

Danmarks Tekniske Universitet
DTU Vindenergi
Nils Koppels Allé
Bygning 403
2800 Kgs. Lyngby

www.vindenergi.dtu.dk

Foreword

MAREWINT is a Marie-Curie Action (2012-2016) Training Network in the multi-disciplinary area of Offshore Wind Turbine engineering focusing on issues having a major impact on their mechanical loading.

More information about the project can be found on the website, www.marewint.eu

Work Package 1 focuses on the rotor blades, defining the challenges for large offshore wind turbines and proposing an innovative response to address these. Work carried out by two researchers within the network that supports the implementation of the new operating concept is summarised here. The first is Gilmar Pereira, based at DTU Wind Energy; the second is Vladimir Leble, based at the University of Glasgow (previously Liverpool).

Risø Campus, DTU Wind Energy, Roskilde, DENMARK
November 2015

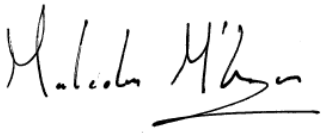

Malcolm McGugan
Senior Development Engineer
MAREWINT Work Package Leader WP1

Contents

Summary

The offshore wind energy industry faces many challenges in the short to medium term if it is to meet the ambitions of the global community for sustainable energy supply in the future. Not least among these challenges is the issue of rotor blades. Innovative design for “smart” rotor blades with embedded sensors and actuation are being developed that will deliver an improved whole-life performance, and a structural health management based operational concept.

In this report, the work of two early stage researchers within the Initial Training Network MAREWINT is presented that support the innovative concept development for wind turbine blades. This covers models and experiments with damage measurement systems embedded within the composite material/structure and numerical methods investigating the effects of leading and trailing edge flaps on modifying the aerodynamic loads on the operating rotor.

1. Introduction

The MAREWINT project (Grant agreement number 309395) was approved for funding as an Initial Training Network within the Seventh Framework programme on 27/06/2012. The full project title is “MAREWINT, new Materials and Reliability in offshore WINd Turbine technology”.

One of the strategic objectives for the Wind Energy Industry is the reduction of the total cost of energy by improving the reliability of wind turbine components and optimising the operation and maintenance strategies. Achieving this would have a direct effect on the availability of the turbines and thus reduce cost while increasing energy output. This would be a major contribution to making wind energy fully competitive, especially in the offshore sector where Operation and Maintenance represent a high percentage of total costs.

Partners:	
Institute of Fluid Flow Machinery PASci (**IMP PAN**)	Poland
Technical University of Denmark (**DTU**)	Denmark
Energy Center Netherlands (**ECN**)	Netherlands
Ship Research and Design Center S.A. (**CTO**)	Poland
University of Liverpool (**LIV**)	United Kingdom
LMS International (**LMS**)	Belgium
Numerical Mechanics Applications International (**Numeca**)	Belgium
TWI LIMITED (**TWI**)	United Kingdom
Norwegian University of Science and Technology (**NTNU**)	Norway
World Maritime University (**WMU**)	Sweden
Relex Italia SRL (**Relex**)	Italy
Katholieke Universiteit Leuven (**KU Leuven**)	Belgium
Associated Partners:	
SSP Technology A/S	Denmark
ZF Wind Power Antwerpen NV	Belgium
Gdansk Shipyard	Poland
FiberSensing	Portugal
Axym Limited	United Kingdom
National Renewable Energy Centre	United Kingdom
Fundación Centro Tecnológico de Componentes	Spain
Academic Computer Centre in Gdansk	Poland
Università degli Studi di Ferrara	Italy
Norwegian Marine Technology Research Institute	Norway

Table 1: List of Partners and Associated Partners in MAREWINT

MAREWINT contributes to this objective by providing training for 14 researchers completing their doctoral programmes in the multidisciplinary area of Offshore Wind Turbine (OWT)

engineering. In particular there is focus on the mechanical loading of OWT components as this is an area that is not yet fully understood. The official MAREWINT project start date was 01/10/2012 and a kick-off meeting attended by all partners and hosted by the project co-ordinators, the Institute of Fluid Flow Machinery - Polish Academy of Science (IMP PAN) was held in in Gdansk on 22-23/10/2012. As can be seen in Table 1, there are 12 participants (beneficiaries) in MAREWINT and 10 associated partners. The total consortium shows a good distribution across Europe and contains 6 Universities, 6 Research Institutes, 4 Small to Medium sized Enterprises (SMEs), and 6 larger Industry partners.

Training activity	**Description**	**Date**	**Venue**
Opening Lecture series	Dynamic modelling and analysis of wind turbine systems	June 2013	NTNU (Norway)
1st Technical Workshop	Basic principles of aerodynamics	September 2013	ECN (Spain)
1st Training Course	Applications of RANS to wind turbine support hydrodynamic predictions	January 2014	Numeca (Belgium)
2nd Technical Workshop	Design for Reliability	May 2014	Relex (Italy)
3rd Technical Workshop and Mid-term Review	Finite Element Method	June 2014	IMP PAN (Poland)
Graduate School	Innovative technologies for Energy Conversion	November 2014	KU Leuven (Belgium)
4th Technical Workshop	Wind turbine CFD	March 2015	Liverpool University (UK)
5th Technical Workshop	Planning, Installing, Operating and Decommissioning of OWT farms	September 2015	DTU (Denmark) WMU (Sweden)
Autumn School	Structural Health Monitoring methods based on elastic wave propagation	November 2015	IMP PAN (Poland)
6th Technical Workshop	Uncertainty Quantification and probabilistic modelling for composite structural analysis. Training courses in MBS: Standard: Basic and advanced, flexible bodies.	March 2016	LMS (Belgium)
Final Network Conference	Final Conference/ More Reliable Offshore Wind Turbine	September 2016	IMP PAN (Poland)

Table 2: List of Network-wide training activities in MAREWINT

MAREWINT is a 48 month project (ending 30/09/2016) with a total budget of 3,822,763 Euro that is allocated among the 12 beneficiaries according to the placement of 14 Early Stage Researchers (ESRs). The 48 months of the project are roughly blocked into three main parts; the first six months for a Recruitment phase where the Partners search for candidates for the 14 available ESR positions, the main research phase (lasting three years), and a final six-month

phase for reporting. All the research, training, management, and dissemination activities of the 14 ESRs are covered by the Project Grant.

A major aspect of the Network interaction in MAREWINT is the series of training events, workshops and conferences arranged throughout the 48 months of the project. OWT engineering is a highly multi-disciplinary field encompassing mechanical engineering, materials science, fluid mechanics, harsh environment engineering, condition monitoring, maintenance, and safety regulations. The aim was therefore to provide a structured, integrated and multi-disciplinary training program for the future OWT technology experts based on a common research programme. An organisation, shown in figure 1, was defined based on five cross-linked Work Packages (WPs) with shared Dissemination/Outreach and Management/Training organisation.

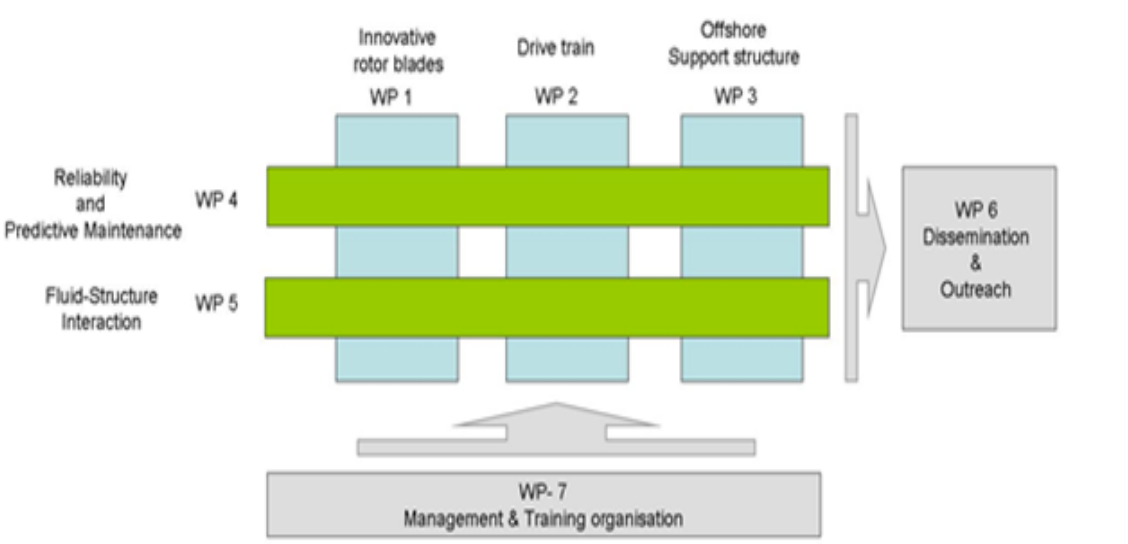

Figure 1: Diagram showing the cross-linked MAREWINT Work Packages

As can be seen in figure 1, the first three (vertical) WPs focus on the major structural components of the OWT; Blades, Drive train, and Support structure. WP 4 and 5 provide the consolidating (horizontal) activities on Reliability / Predictive maintenance and Fluid-Structure Interaction respectively.

In WP1 structural and fluid dynamics investigations on the rotor blade are approached by numerical and experimental methods. Within the work package two individual projects were developed, the first considering the behaviour of the composite material (particularly when in damaged condition) within the blade structure and the use of embedded sensors to detect this behaviour, and the second describing structural behaviour and rotor performance in Computational Fluid Dynamics models, including the use of leading and trailing edge flaps to modify this. These activities cross-link with the combinatory horizontal work packages by providing, among other things, structural health information to the reliability and predictive maintenance work package, and input to the fluid-structure interaction models developed for the entire turbine.

MAREWINT WP1 was led by the DTU Wind Energy department with ESR1 (Gilmar Periera) based at DTU and ESR2 (Vladimir Leble) based at Liverpool University (later Glasgow University).

In order to provide a common platform for the Work Packages a reference model was agreed as one of the first deliverables in the project (WP5, D.5 Definitions of the reference wind turbine data, DTU, M6). Described by [Bak2013], the DTU 10MW reference wind turbine was developed by DTU Wind Energy together with Vestas Wind Systems as part of a collaborative research intended to create the design basis for the next generation of wind turbines. As such it is an ideal, publically available reference for MAREWINT to work on the optimisation of large offshore wind installations.

Description	**Value**
Rating	10MW
Rotor orientation, configuration	Upwind, 3 blades
Control	Variable speed, collective pitch
Drive train	Medium speed
Rotor, Hub diameter	178.3m, 5.6m
Hub height	119m
Cut-in, Rated, Cut-out wind speed	4m/s, 11.4m/s, 25m/s
Cut-in, Rated rotor speed	6rpm, 9.6rpm
Rated tip speed	90m/s
Overhang, Shaft tilt, Pre-cone	7.07m, 5˚, 2.5˚
Pre-bend	3m
Rotor mass	229 tons (each blade 41 tons)
Nacelle mass	446 tons
Tower mass	605 tons

Table 3: DTU10MW Reference Wind Turbine design summary from Bak et al. (2013)

The objective of this report is, firstly, to introduce the MAREWINT organisation and the motivations for the consortium; in particular the key shared Network resources of:-

- training course series
- a common research program
- and reference model

Secondly to present the Industry situation with respect to innovative rotor blades for large offshore wind turbines and the concept of operation proposed by the authors for using these smart structures in the future. And finally to report the work of the Early Stage Researchers in Work Package 1 that supports the development and implementation of this concept.

2. Innovative Rotor Blades

Being an essay on the concept for Innovative Rotor Blades in three parts…

1. What is the situation (with Blades) for offshore wind turbines?
2. How do we propose to react to this?
3. Operational concept

2.1 Current situation and trends

Access to affordable, reliable, sustainable and modern energy is one of the 2030 targets for the United Nations (https://sustainabledevelopment.un.org/topics). This requires a substantial increase in the share of renewable energy within the global energy mix, and wind is a prominent part of the solution if the world is to achieve such a target. The potential for offshore wind energy is enormous with industry projections in Europe showing an increase from 5GW in 2012 to 150GW in 2030 (European Wind Energy Association figures, www.ewea.org). By moving to offshore sites the Industry can establish larger wind farms with turbines of a size that would not be easily accepted onshore where land use is at a premium. In addition to this, the quality of the wind resource is greatly improved away from the effect of land contours, forests, and so on.

However, moving such a large portion of the Industrial production capacity offshore is a major challenge. The environment offshore can be extreme and requires a more robust and durable design for all components, access is expensive for establishing and maintaining production offshore, and support structure designs for deep water sites are yet to be proven commercially. At EWEA 2014, the most important industrial offshore wind energy conference, the delegates were warned that without a reduction in energy costs corresponding to at least 40%, offshore wind could not persist in the current energy market beyond 2020 (EWEA 2014 newspaper, Recharge – day three). While costs for onshore wind are already competitive, targeting a reduction in the cost of energy offshore was vital if the ambitious political and industrial targets are to be achieved. It was further observed that initial offshore developments were based on technology from the offshore oil and gas supply chain which is driven by a need to maximise production, rather than by cost reduction. The solution agreed was for a more focussed investment in research and development that produces innovations in logistics, transport and operation.

One of the most eye-catching developments in the wind energy industry over the last fifteen years has been the increase in the size of the turbines being manufactured with new turbine designs consistently providing larger turbines with higher power ratings.

Year	Manufacturer (rotor diameter)	Effect	Tip height
2000	Vestas Wind Systems V52	2.5 MW	70m
2015	Vestas Wind Systems V164	8.0 MW	222m

Table 4: Comparison example between commercial turbines developed in 2000 and 2015

As the rotors become larger, the industry has relied on improvements in blade structural design, manufacturing processes and material properties in order to meet the requirements for ever longer blades that remain light-weight, strong and stiff. It can be argued that the blades present the most challenging materials, design and engineering problems being a complex, anisotropic material in an aerodynamic structure that is subjected to continuous dynamic loadings of a combined and non-uniform nature over long periods of time. These operational requirements and conditions lead to materials that must exhibit a high stiffness, a low density, and long fatigue life.

Material performance criteria therefore identify fibre reinforced polymer composites as the prime candidate for rotor blades. Here the stiff fibres (usually glass, sometimes carbon) are aligned in the primary load directions within a cured matrix of resin (usually thermosetting polyester or epoxy). The processing technology for such material (whether pre-preg, resin infusion, or wet layup) involves considering the material properties, design approach and manufacturing process as an integrated issue as already at this stage the characteristics of the material (and hence the behaviour of the final structure) are determined. For example, in longer rotor blades the reinforcing (stiffening) fibres must be aligned along the length of the blade, but with sufficient understanding of the out-of-plane properties and weak laminate interfaces and bond lines so as not to generate problems with durability when the complex combined loads are encountered.

Blade design combines a relatively thin shelled aerodynamic profile supported by a longitudinal beam or webs which carry the bulk of the structural load. The blades are heavier at the root section and taper towards the tip to match the load distribution in a cantilever beam structure and maintain the allowed material strain levels. Industry demands have spurred improvements in design with an optimised aerodynamic profile, relative reduction in weight for longer blades and integrated bend-twist coupling into the structural response.

The design philosophy for rotor blades (as with all fibre reinforced polymer structures) began with large safety factors and addressing simple issues of linear elastic behaviour. With time, as knowledge about the materials, structural behaviour and manufacturing approaches increased (coupled with the pressure to make more daring multi-MW designs) it became possible to adopt more advanced structural design approaches. The development in light weight structure design is nicely illustrated in a general way by [Braga2014]. Thus we see that an implementation of “smart” structure technology is the anticipated innovation to supersede the current state of the art.

Summarising we see a trend in the wind energy industry for:-

- a rapid increase in the level of installed capacity world-wide
- an increase in the physical size (dimensions) of the structures
- an increase in the size (number of multi-MW turbines) of individual wind farms
- a tendency to place these wind farms offshore
- higher industry requirements for reliability, safety and easy maintenance
- a strong focus on a reduction in the cost per “unit” of energy produced
- new materials, designs, and production methods continuously adopted

2.2 The proposed response

As the most effective way to increase the power produced per turbine is to make each turbine bigger, we now have an industry that manufactures extremely large rotor blades using low-cost fibre composite material and low-cost manufacturing methods. A consequence of the components in a wind turbine blade being so large (in some companies almost the entire structure is manufactured in one piece via resin infusion of dry laminate layers), is that there is little scope for improving the performance of a finished blade by rejecting parts that do not meet very high quality standards. This is because the low-cost manufacturing approach demanded by the industry makes manufacturing a “perfect” blade challenging, and parts thus rejected would be too costly to simply discard.

Instead the situation is that each blade has a unique set of “variations” (we might call then defects) from the intended “perfect” design; these are then more or less mitigated with repair technology before leaving the factory. And in operation the specific load profile will also vary for each turbine. Without detailed information about the distribution of structural/material defects and repairs present combined with detailed loading and response history for each blade it will be impossible to make accurate predictions about the lifetime performance of these blades individually; only a generalised probability analysis. And prescribing regular manual inspection is neither an economical nor technically efficient solution as offshore this would be both costly and difficult.

A full understanding of each individual stage in the wind turbine blade operational life, such as manufacturing, operational, emergency situations, repairing, etc., is therefore not enough to achieve a smart wind turbine blade concept. Knowledge of how each stage interconnects with the processor and successor, and the impact of a change in any properties in to the wind turbine blade operational life is required.

The traditional Mono-Stage design and methodology as shown in figure 2, is no longer applicable to match this requirement; especially as blades become larger, more complex and expensive to manufacture, more information feedback is required to maximise their lifetime and improve processes.

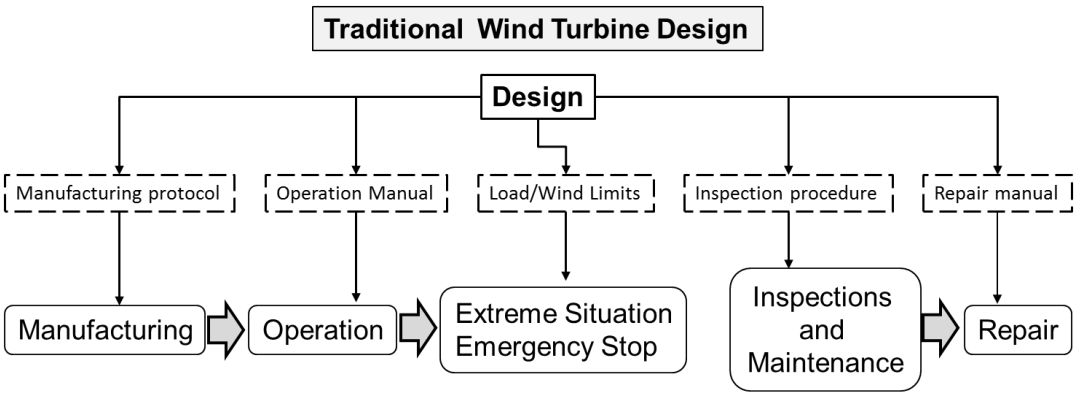

Figure 2: Life stages of a wind turbine blade: traditional design methodology.

Thus, methods to measure and evaluate structural integrity and operational parameters through all the wind turbine blade life stages need to be implemented from the design stage [McGugan2015].

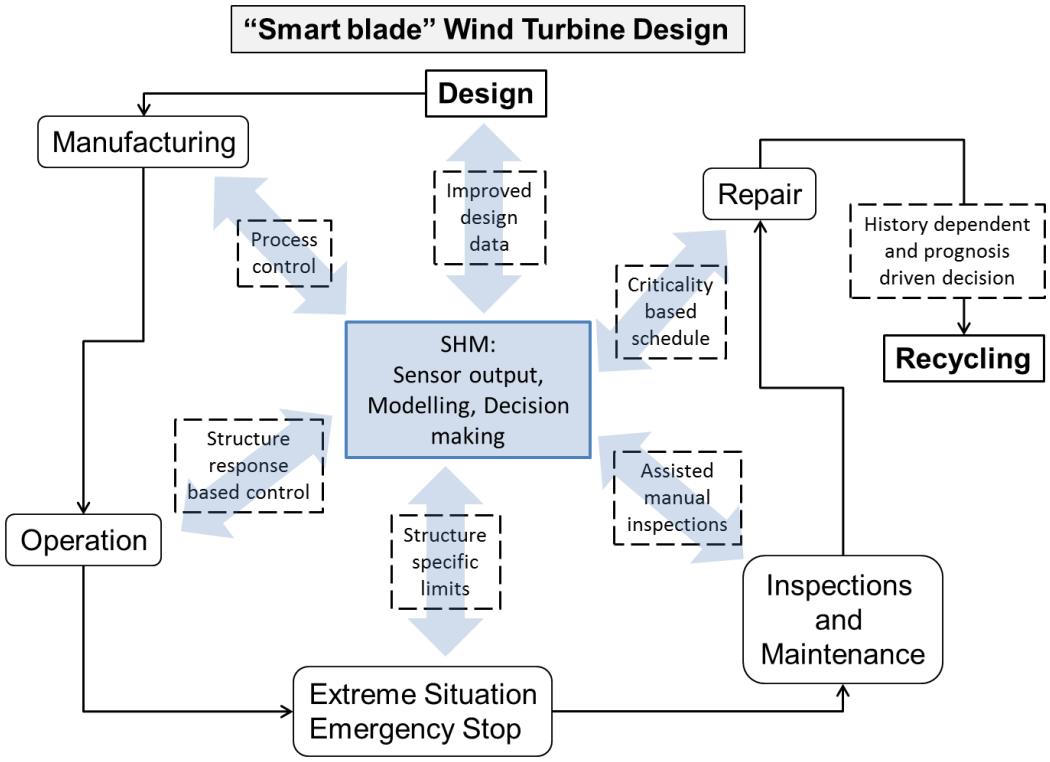

Figure 3: Life stages of a wind turbine blade: "smart blade" design methodology.

The smart blade design and methodology is shown in figure 3. The presence of sensors integrated in the structure since manufacture will provide feedback at each stage of the structure life time. For example, if during an extreme load a change in the material stiffness is detected, caused by delamination or a crack in the adhesive joint, the wind turbine operation limit can be decreases based on this information. This will enable the structure to operate safely until the next repair action, continue to generate energy and minimizing monetary loses.

Structural Health Monitoring is a well-known engineering area concerned with assessing the current state of a specific asset in order to ensure proper performance. It has the perspective to function both as an automated (and remote) maintenance and inspection process, as well as a "smart" structure feedback allowing activation and response based on condition and environment.

The novel approach proposed is thus that blades are allowed to contain defects and develop stable damage under operation as under current "passive" damage tolerant design philosophy. But the implementation of structural feedback from the embedded sensors and active response (described in the next section) is combined with improved damage tolerant design materials and design methods to expand the current design philosophy to include SHM and applied fracture mechanics and ensure that defects cannot develop into unstable damage leading to blade failure. Furthermore, a full life-time perspective is given that enables a holistic optimisation of the structural resources.

2.3 Operational concept

Although many sectors share similar ambitions regarding polymer composite structural materials, structural diagnosis, and prognostic approaches, each one will differ in how they exploit the new technology and apply the new developments. The different expectations and priorities across the Industrial sectors will influence the entire design, processing, and maintenance line. For example, the aerospace sector can be characterised by polymer composite structures that are high cost material and high value structures, whereas the wind energy sector considers the rotor blades as low cost material and high value structure. This means that a common “toolkit” of deliverables and work areas exist for defining a physics-based polymer structural component life analysis that can be investigated by researchers and industry across different sectors. However from this “open-source” framework, sector specific implementations will be developed.

The upper part of figure 4 shows the concept of a blade structure usage being “consumed” during operation in a more or less controlled and progressive manner throughout the planned service life. The usage depends on the load input which is monitored, understood and controlled (active management) to a greater or lesser extent. This could begin via a simple measurement of wind speeds and a calculation of aerodynamic loads on the structure resulting in a “cut off” wind speed above which the turbine does not run (in part to avoid overload situations). Progressively more advanced designs including passive bend-twist blades, active control of pitch and trailing edge settings combined with turbine specific in-flow measurement allows for load alleviation from tower shadow effects, shear loads, turbulence, and so on. The degree of structure control available effects the load spectra applied and defines the risk of peak loads that will progress (or initiate) damage. The greater the degree of control, the more availability a damaged structure can exhibit. The availability of a distributed in-situ load monitoring capability will enhance aerodynamic load control options.

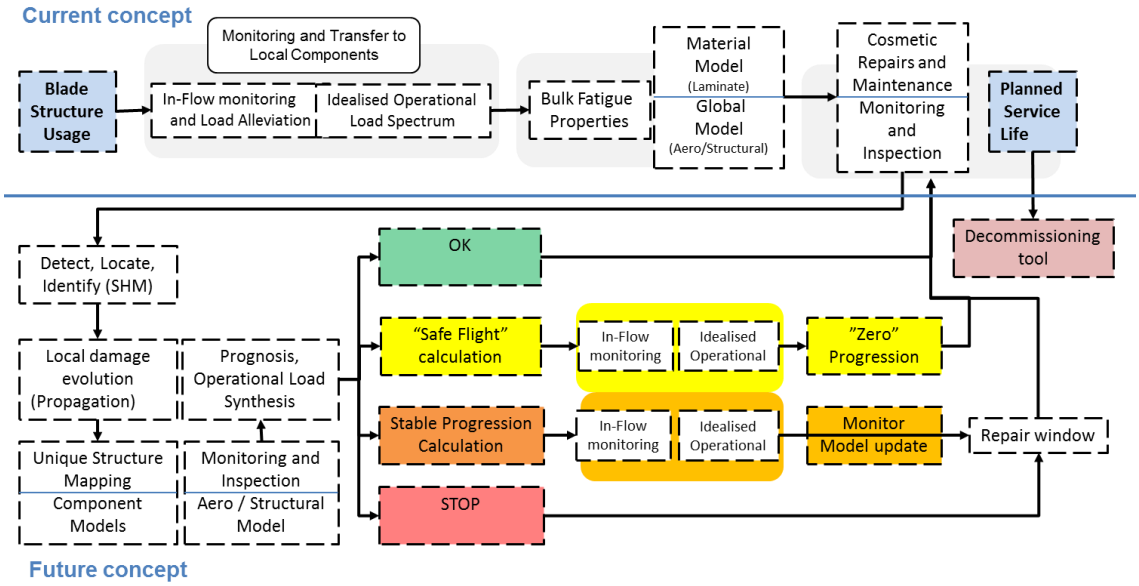

Figure 4: Health Management Concept for future Innovative Rotor Blades

Moreover, combining Structural Health Monitoring with other inspection technology will detect and characterise localised damage for each structure, generating a “damage map” for each wind turbine blade with local and global damage models communicating to define critical (and sub-critical) failure criteria. A prognosis tool based on the local forecast of operation can propose the suitable structural sustainment action:-

- an unaltered operation (exploiting the passive/designed damage tolerance capability of the material/structure)
- a modification of the structure control settings to limit load conditions that risk progressing damage (a “safe flight” operation)
- an operation of the structure that will allow a progression of damage but in a stable regime allowing repair to be scheduled for the next available maintenance period
- or an immediate stop pending critical repair

In all cases the target for the individual structures is to meet the planned service life whereupon “problem” structures can be decommissioned, and the remainder assessed for the feasibility of an extended operational lifetime. The updated database of structural integrity information generated by this process improves the decision making regarding which structures can be safely licensed for continued operation, and those that need refit, resale, or recycling.

3. Fibre Bragg grating as a multi-stage structure health monitoring sensor

There is a clear need to implement models and measurement systems through the entire life of the wind turbine blade. In this chapter will be presented some work conducted to implement optical fibres as a multi-stage sensor, capable to measure different structural properties, and link them with all the different life stages and support a better design of the wind turbine blades. We will focus in the two first stages: the manufacturing stage and the operational stage.

3.1 Fibre Bragg grating sensors

Fibre Bragg grating (FBG) sensors are the most commonly used type of sensors in the fibre optic field. An FBG sensor can be embedded in the Fibre reinforced polymer material (main material of the wind turbine blade), without compromising its structural resistance. This is due to the FBG reduced size, with a diameter of $125\ \mu m$ it is virtual non-intrusive to the material. Also, FBG sensors present other interesting features, such high resolution, multiplexing capability, immunity to electro-magnetic fields, chemical inertness and long term stability.

A FBG is formed by a permanent periodic modulation of the refractive index along a section of an optical fibre, by exposing the optical fibre to an interference pattern of intense ultra-violet light. The photosensitivity of the silica exposed to the ultra-violet light is increased, so when light propagates through the periodically alternating regions of higher and lower refractive index within the fibre, it is reflected by successive, coherent scattering from the index variations. When the reflection from a crest in the index modulation is in phase with the next one, it is generated

the maximum mode coupling or reflection. The strongest mode coupling occurs at the Bragg wavelength, λ_b, as shown in figure 5. The wavelength λ_b, is described by the Bragg condition,

$$\lambda_b = 2n_{eff}\Lambda \tag{1}$$

where n_{eff} is the mean effective refractive index at the location of the grating and Λ is the constant nominal period of the refractive index modulation. [Hill1997]

The bandwidth $\bar{\lambda}$ (distance between the two first minima) is given by,

$$\frac{\bar{\lambda}}{\lambda_b} = \frac{1}{n_{eff}}\sqrt{\left(\zeta\overline{\delta n_{eff}}\right)^2 + \left(\frac{\lambda_b}{L}\right)^2} \tag{2}$$

where *L* is the gauge length, $\overline{\delta n_{eff}}$ is the mean induced change in n_{eff} and ζ is the amplitude of the induced index change [Peters2001]. An external load or temperature variation will change the effective index of refraction and/or the period of modulation; this will create a shift of the wavelength reflected peak from its original value.

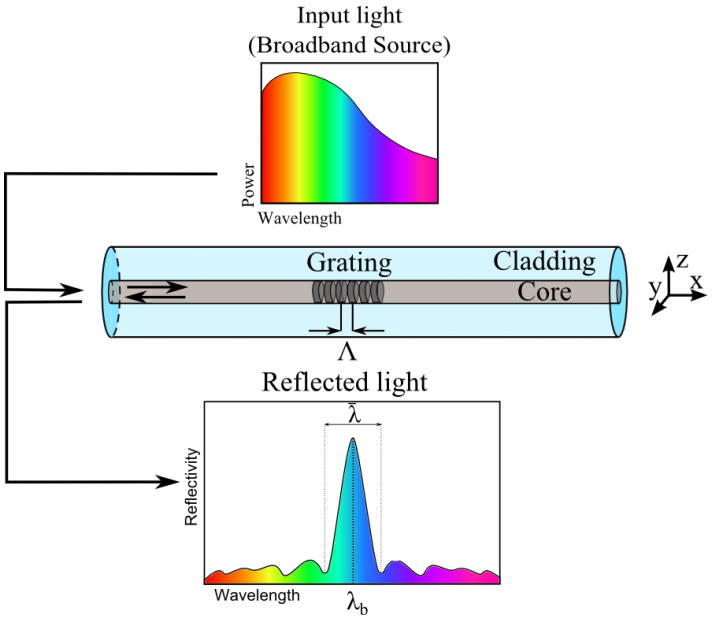

Figure 5: Fibre Bragg grating: strongest mode coupling at the Bragg wavelength.

3.2 Manufacturing stage: residual stress induced by resin shrinkage and curing process control

The FBG sensors are an excellent choice to monitor the curing process of wind turbine blades, where their capability of surveying the curing process is combined with their capability to monitor strain and other features over the structure lifetime. Because the FBG sensor small size that makes them virtually non-intrusive to the structure, they can be embedded in the composite layers from the first manufacturing step. This embedded sensor will monitor several parameters of the curing process: temperature of the resin, which enables a retro-feedback of temperature to the process controller; residual stress that are a big issue in the fatigue performance of the

composite; Resin flow, by measuring the position of dry spots in the laminate; etc. Plus, the FBG sensor can be used as part of the process certification, by giving information about the curing profile of the structure, the residual stress, the load history during manufacturing, transport and installation.

3.2.1 Embedded FBG response to strain and temperature variation

Assuming a perfect strain transfer between an embedded FBG sensor and the host material, the wavelength shift, $\Delta\lambda_b$, under variation of strain in the longitudinal direction of the fibre optic, ε_1, and temperature, ΔT, is given by the equation (3).

$$\frac{\Delta\lambda_b}{\lambda_b} = (1 - p_e)\varepsilon_1 + [(1 - p_e)(\alpha_s - \alpha_f) + \xi]\Delta T \quad (3)$$

The parameter p_e is the optical fibre photo-elastic coefficients, α_s and α_f are the thermal expansion coefficient of the host material and the optical fibre, respectively, and ξ is the thermos-optic coefficient [Magne1997].

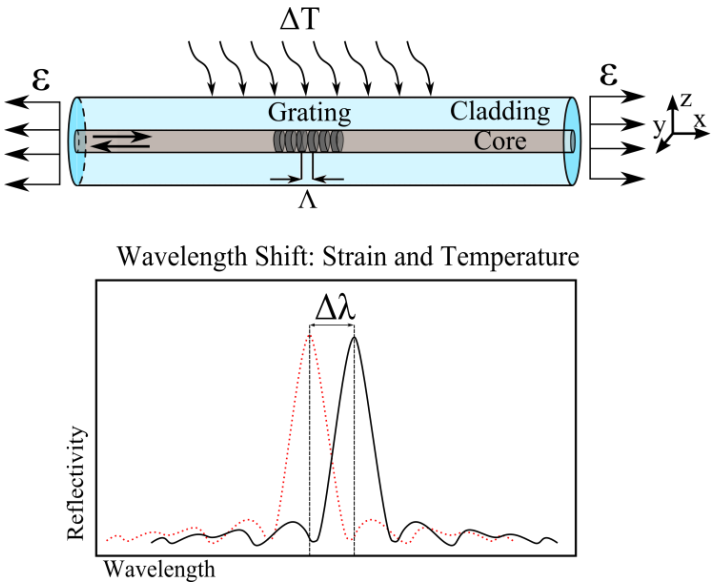

Figure 6: Fibre Bragg grating response: strain and temperature variation.

3.2.2 Residual Stress Measurement

Curing cycles are often defined on the basis of experience and economical aspects, missing the opportunity to improve curing cycles and blades, by understanding the physic-chemical process. Reducing the reaction time by increasing the temperature leads to a decrease in production time and consequent lower production cost. But this can lead to residual stress induced by the curing process, which causes worst mechanical properties and reduces the fatigue life of the structure.

The equation (3) was rewritten to measure the residual stress caused by the material shrinkage:

$$\varepsilon_{shrinkage} = \frac{\frac{\Delta\lambda_b}{\lambda_b} - \xi\Delta T}{1 - p_e} + \alpha_f \Delta T \quad (4)$$

By measuring the temperature in the resin using a thermocouple, is possible to decouple the temperature-strain cross sensitivity of the FGB and calculates the epoxy shrinkage.

3.3 Operation Stage: crack growth detection by embedded FBG sensors.

Often in fibre reinforced polymers (FRP), delamination is accompanied by the formation of a crack bridging zone, where intact fibres connect the crack faces behind the crack tip, as shown in figure 7. Thus, the energy required for the crack to propagate is higher than required to initiate. The relationships between the crack bridging stresses and the crack opening displacement (bridging laws) are used to describe the effect of fibres on the crack propagation [Sørensen2010]. The cracking in homogeneous isotropic materials usually occurs under pure Mode I (opening loading) but in weak planes or along interfaces, like in composite materials cracking, occurs under a combination of Modes (Shear and opening loading).

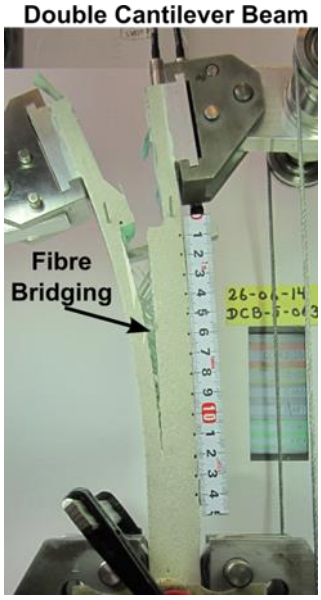

Figure 7: Fibre bridging during delamination of a DCB specimen

In order to detect delamination/crack in FRP materials the sensor/monitoring system need to track specific fracture features that only appear in the vicinities of the crack, independent of geometry and loading conditions. Thus, to link these fracture features with the measured parameters, the strain distribution around a crack tip during delamination was analysed using Digital Image Correlation (DIC), as shown in figure 8 *[Gilmar2015-DAMAS]*. The DIC technique is a non-contact optical method that, by tracking changes in a random pattern on the specimen, can correlate it with deformation/strain of the material.

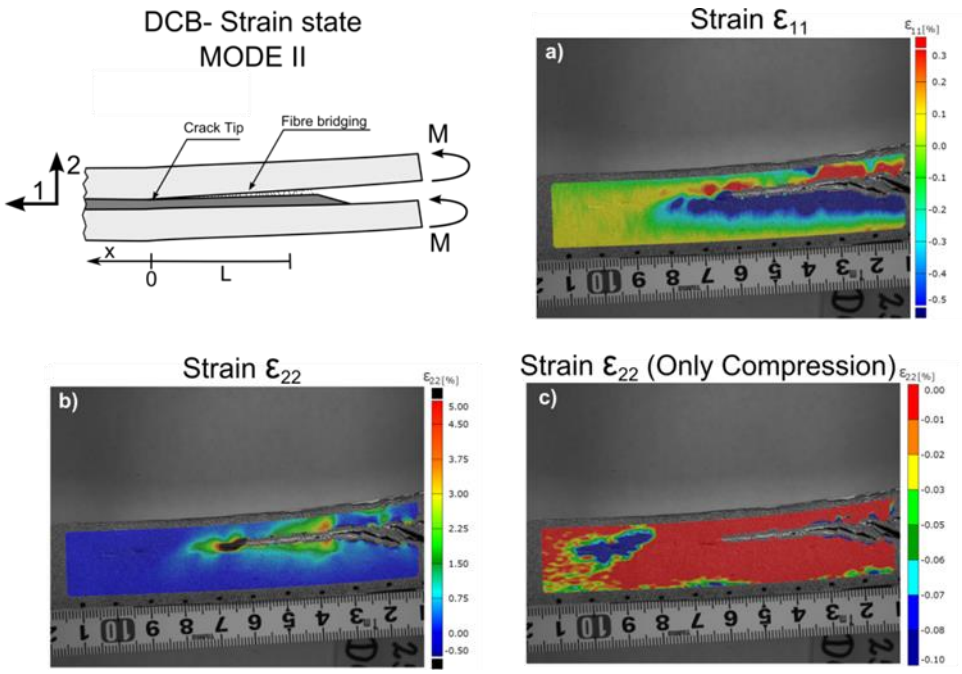

Figure 8: Strain distribution at the crack tip during Mode II fracture [Gilmar2015-DAMAS].

It is possible to divide the strain distribution in two distinct contributions: crack tip singularity/material damage and fibre bridging. Near the crack tip, the stress field closely approaches the singular stress field of linear elastic fracture mechanics. This means that the stress tends to infinity and has a fast variation (high gradient). Also, with the progression of the crack the material/structure losses stiffness increasing the strain, here it is possible to observe higher values of strain ε_{11} at the crack faces, as showed in figure 8a). In the fibre bridging zone (L<x<0), a positive strain $\varepsilon_{22}$was observed, due to the forces transferred by the fibre that are connecting the two crack faces, as shown in figure 8c). These forces are balanced by a compression stress that appears ahead of the crack tip (x>0), which creates a negative strain ε_{22}, shown in figure 8c) as a blue area.

3.3.1 Crack/Delamination detection by embedded fibre Bragg gratings

As measured using DIC technique, during a crack/delamination event different fracture features will be present near the crack tip. Being able to identify and measure these specific phenomena with a FBG sensor is the key factor to correctly determine the presence of damage and it growth.

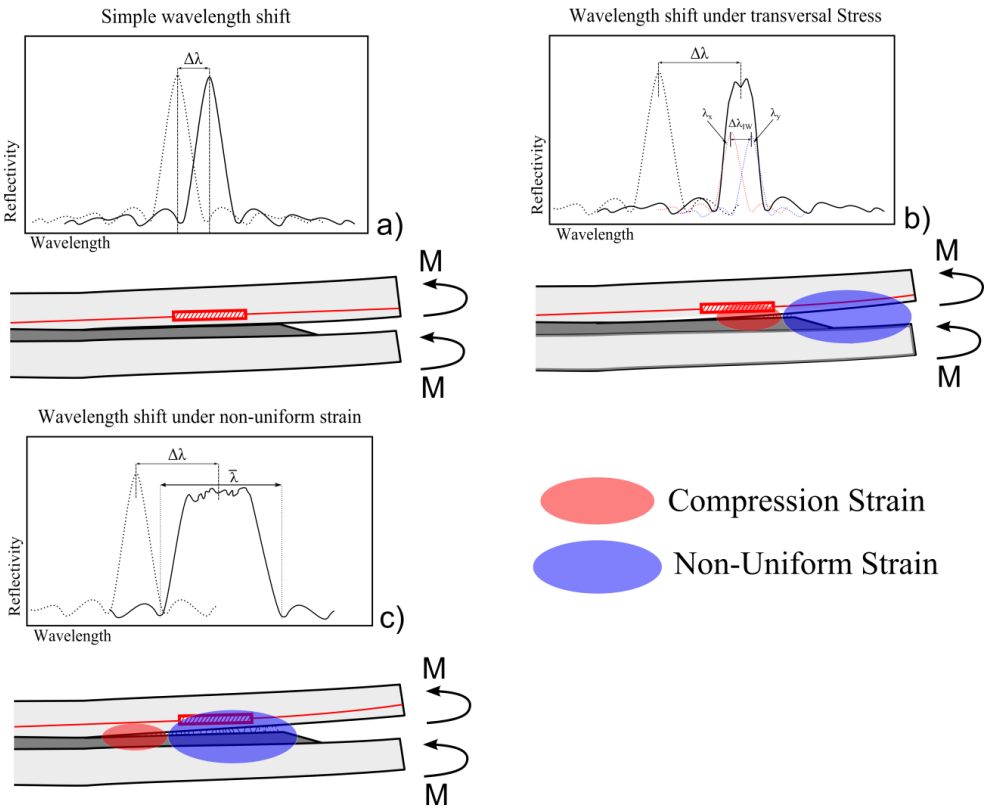

Figure 9: Stages of the FBG response under a crack growth event.

The three different stages of the FBG responses under a crack growth event are presented in figure 9. First, before the crack reaches the proximity of the grating (figure 9a)), the material will build-up strain, that will create a uniform wavelength shift in the FBG reflected peak. Next, a compression field is formed ahead of the crack tip due to the formation of a crack bridging zone (figure 9b)). When this compression field reaches the grating area it creates a peak splitting of the FGB response. Then, when the grating is near the influence of the crack singularity (figure 9c)), a non-uniform strain field will also modify the shape of the reflected peak. After the crack passes the FBG sensor, the shape of the reflected peak will go back to the original shape, and the sensor response will again be a simple wavelength shift, because at this stage only uniform strains will be present at the FBG.

Embedded FBG response: Strain

As mentioned before, the FBG response to strain and temperature variation can be described by equation (3). However, during crack growth the temperature variation can be neglected. The wavelength shift $\Delta\lambda_b$ (figure 7a)) is given by equation (5).

$$\frac{\Delta\lambda_b}{\lambda_b} = (1 - p_e)\varepsilon_1 \tag{5}$$

Embedded FBG response: Transverse Stress

The compression field formed ahead of the crack tip will reach the grating area, which will create a peak split of the FBG reflected signal (figure 7b)). This peak split phenomenon is due to a birefringent effect, which can be defined as the change of the refractive index n_{eff} in the

two directions n_{effy} and n_{effz}, when the grating is subjected to a transverse force [Sørensen2007, Jülich2010]. The increase in the width of the reflected peak, $\Delta\lambda_{wv}$, is given by the equation 6,

$$\Delta\lambda_{wv} = 2\Lambda\left|\Delta n_{effy} - \Delta n_{effz}\right| = \frac{\Lambda n_0^3}{E_f}\left[(1-\nu_f)p_{12} - (1+\nu_f)p_{11}\right]\left|\sigma_y - \sigma_z\right| \quad (6)$$

where $\sigma_{y,z}$ is the transverse stress, E_f is the elastic modulus of the optical fibre, ν_f is the Poisson's ration, n_0 is the initial refractive index, p_{11} and p_{12} are the photo-elastic coefficients of the optical fibre.

Embedded FBG response: Non-Uniform Strain

A non-uniform strain changes the periodicity of the grating pattern along the sensor length, modifying the grating pattern configuration from "uniform" to "chirped". As demonstrated by Peters [Peters], in a uniform grating the applied strain will induce a change in both grating period and the mean index. These two effects can be superimposed by applying an effective strain of "$(1-p_e)\varepsilon_1(x)$". Then it is possible to rewrite the grating period as:

$$\Lambda(x) = \Lambda_0[1 + (1-p_e)\varepsilon_x(x)] \quad (7)$$

where Λ_0 is the grating period with zero strain. The non-uniform strain effect can be approximated by using the maximum and minimum strain values along the grating. So, the maximum grating period Λ_{max} and minimum Λ_{min} can be calculated using the equation (1). Thus, an approximated increase of the width of the reflected peak due to a non-uniform strain, $\bar{\lambda}$, is given by combining equations (7) and equation (1):

$$\bar{\lambda} = 2n_{eff}[\Lambda_{max} - \Lambda_{min}] \quad (8)$$

3.3.2 Delamination detection in fibre reinforced polymer specimen using embedded FBG sensor: Material and Testing Procedure

To validate the crack detection technique double cantilever beam (DCB) specimens were tested in a fracture testing machine, developed by Sørensen [Sørensen 2010]. The DCB specimens were loaded with different combination of moments, giving different type of fracture modes that simulates different crack/delamination cases. The DCB specimens were manufactured using two FRP material arms, made of unidirectional and triaxial glass fibre layers (SAERTEX UD and TRIAX), with a layup stacking of : [90/ +45 /-45/04/04/+45/-45/90], glued by a commercial epoxy structural adhesive (Epikote MGS BPR 135G/Epikote MGS BPH137G). A thin slip foil was placed in the edge of the structural adhesive, to act as a pre-crack and ease crack initiation.

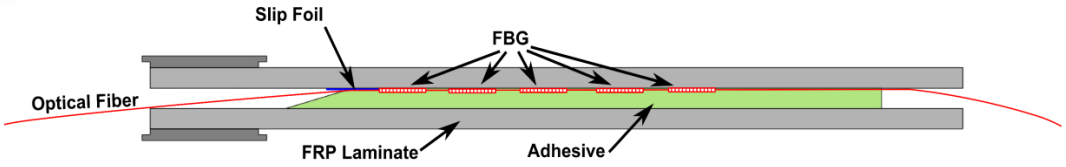

Figure 10: DCB specimen geometry and FBG sensor array configuration.

An array of 5 uncoated single mode (SM) FBG sensors, each with a length of 10 mm, was embedded in the interface of the composite material with the structural adhesive. The gratings array were spaced by 10 mm from each other, and the first grating was positioned 10 mm from the edge of the adhesive. In figure 10, the DCB specimen and FBG sensor array configuration is presented. The sensors were connected to an Optical Spectral Analyser (OSA) FS2200 - Industrial BraggMETER from FiberSensingTM.

Experimental Results

In figure 11 and 12, the strain distribution on the surface of the DCB specimen (left pictures) and the FBG sensor output (right picture), before and during the propagation of the crack/delamination are shown. Before the crack starts to propagate in the material, it is observed a build-up of strain caused by the increase of load. Once the crack start to grow, a compression field is formed ahead the crack tip due to the formation of a crack bridging zone. This compression stress area can be observed in figure 11: top left DIC measurement as a blue spot. At the same time, a decrease in the material compliance due to the growth of the crack causes a rapid local increase of strain, creating a gradient of strain near the crack tip (non-uniform strain), which can be observed in figure 12: bottom left DIC measurement.

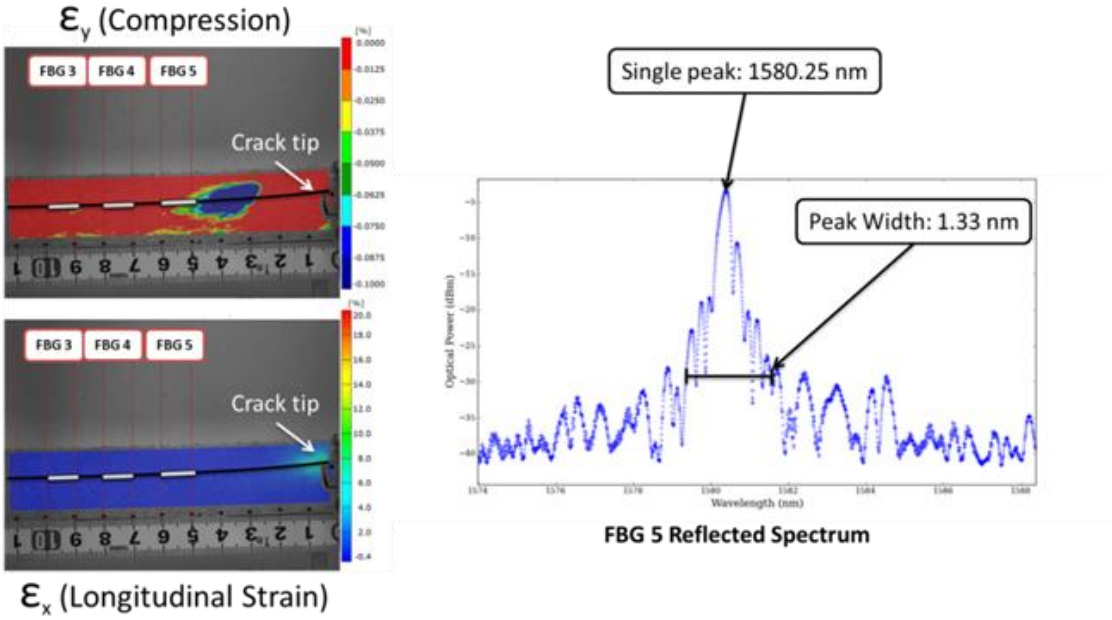

Figure 11: FBG sensor output and DIC measurement before crack growth.

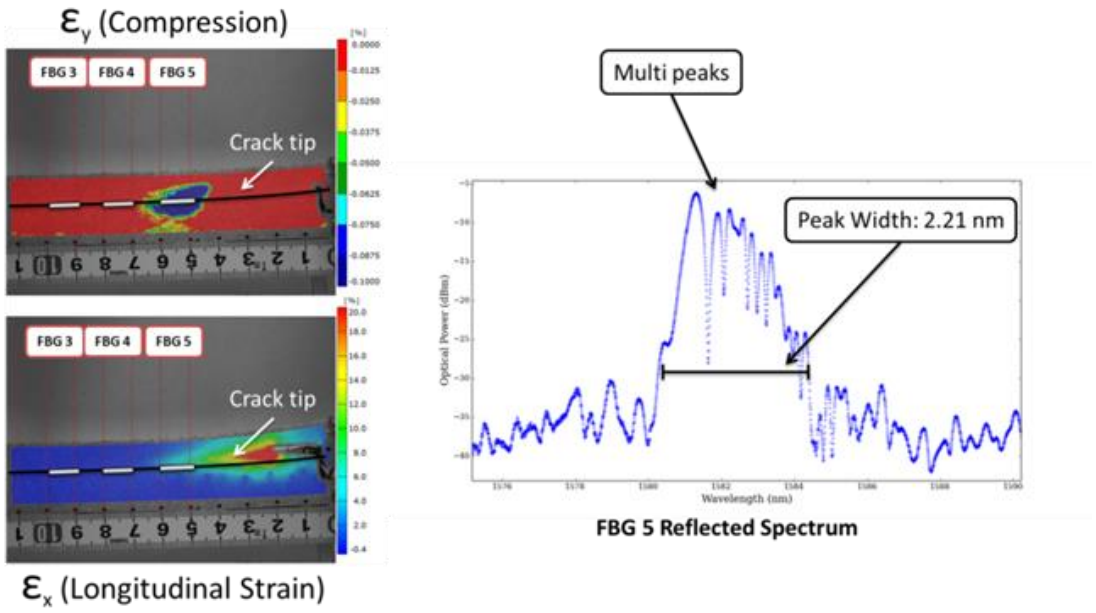

Figure 12: FBG sensor output and DIC measurement during crack growth.

The wavelength shift and peak width at -30dBm, computed from the output of the FBG array in three different loading conditions, is presented in figure 13. The different colours plotted correspond to each Bragg grating in the sensor array. The FBG5 (Orange colour line) is the grating located closest to adhesive edge and the FBG1 (Black colour line) is the grating more distant. The crack growth in the order: FBG 5 →4 →3 →2→1. The wavelength shift is dependent on the loading type, but the increase in the width of the peak is related to the presence of the crack (Birefringent effect and non-uniform strain). Using this information it is possible to track the crack by measure an abrupt variation of the wavelength and/or increase in the width of the reflected peak.

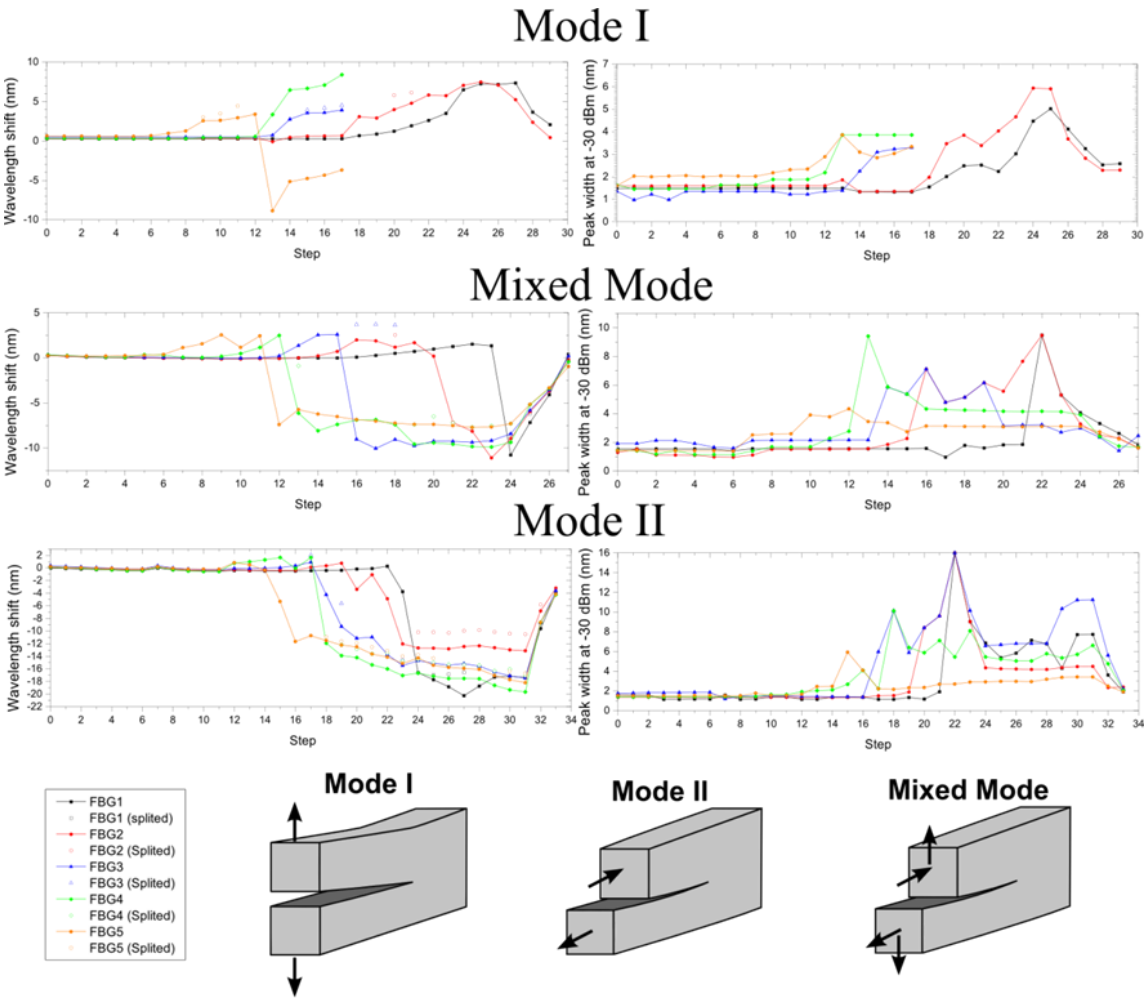

Figure 13: Sensor array output during crack growth.

3.3.3 Application of the FBG Crack detection method

By using this method it becomes possible to extract two types of information from the sensor: one type dependent of the loading and geometry, ε_{zz}, which give information about the global strain/loading state of the structure; The other type, ε_{zz} (z) and $\sigma_{x,y}$, independent and only affected by the proximity of a crack.

To demonstrate the applicability of this technique to other structures or materials, this monitoring method was implemented in a Finite Element Method (FEM) Model of the DCB specimen, which simulates the response of the FBG sensor during the process of the crack growth, as shown in figure 14.

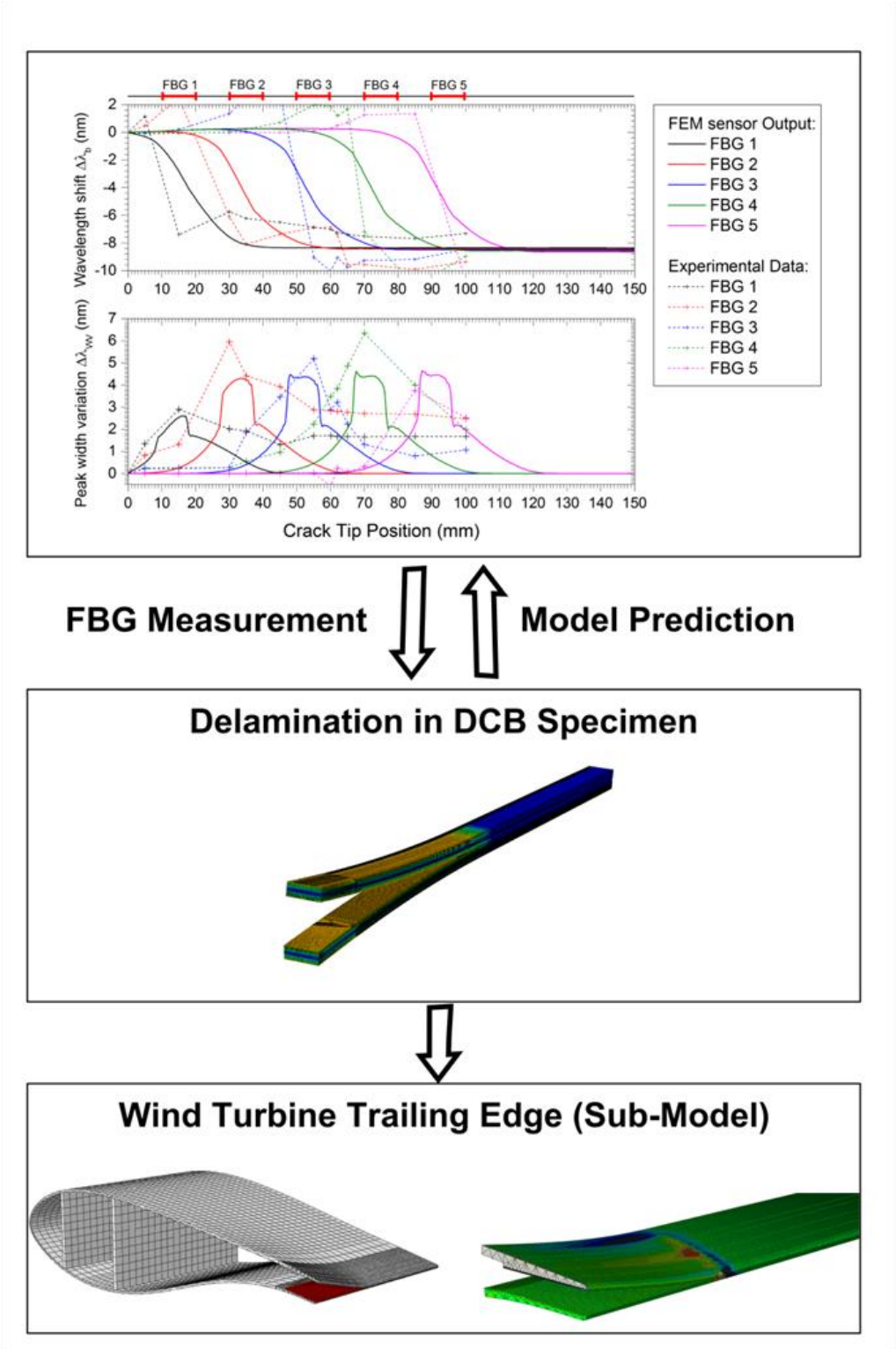

Figure 14: Application of the FBG crack detection method in a DCB specimen and Wind Turbine trailing edge.

3.4 Fibre Bragg grating as a multi-stage structure health monitoring sensor: *Published Work*

- G. Pereira, L. P. Mikkelsen, M. McGugan, Crack Detection in Fibre Reinforced Plastic Structures Using Embedded Fibre Bragg Grating Sensors: Theory, Model Development and Experimental Validation, Journal: PlosOne (Accepted- Under Press revision)
- G. Pereira, L. P. Mikkelsen, M. McGugan, Fibre Bragg Grating Sensor Signal Post-Processing Algorithm: Crack Growth Monitoring in Fibre Reinforced Plastic Structures, Springer Proceedings in Physics (Accepted- Under Press revision)
- G. Pereira, L. P. Mikkelsen, M. McGugan, Damage tolerant design: failure and crack propagation in composites. In *Proceedings of 10th EAWE PhD Seminar on Wind Energy in Europe.* (pp. 1-5). European Academy of Wind Energy
- G. Pereira, L. P. Mikkelsen, M. McGugan, M. (2014). FEM model of Embedded Fibre Bragg Grating Sensor Response: Crack Growing Detection, In Proceedings *NAFEMS NORDIC- Simulation Verification and Validation (V&V): A Key Enabler for Virtual Product Development*, 3 – 4 November 2014, Copenhagen, Denmark
- G. Pereira, L. P. Mikkelsen, M. McGugan, Crack Growth Monitoring by Embedded Optical Fibre Bragg Grating Sensors, In Proceedings of 3rd International Conference on photonics, Optics and Laser Technology, 13-15 March, 2015 Berlin, Germany
- G. Pereira, L. P. Mikkelsen, M. McGugan, Embedded Fibre Bragg Grating Sensor Response Model: Crack Growing Detection in Fibre Reinforced Plastic Material, In Proceedings 11th International Conference on Damage Assessment of Structures-DAMAS, Ghent University, Belgium 24-26 August 2015
- G. Pereira, L. P. Mikkelsen, M. McGugan, Structural Health Monitoring Method for Wind Turbine Trailing Edge: Crack Growth Detection Using Fibre Bragg Grating Sensor Embedded in Composite Materials, In Proceedings 20th International Conference on Composite Materials in Copenhagen, 19-24 July 2015

4. Trailing and Leading edge flaps for Load alleviation and structure control

This section presents the result obtained for the DTU 10MW RWT design by [Bak2013]. The section is divided in the description of employed numerical methods, mesh convergence study, and the rigid blade cases with trailing and leading edge flaps. For all presented test cases density of the air was assumed to be ρ=1.225kg/m^3, the dynamic viscosity of the air was assumed to be μ=1.8·10-5 N·s/m^2, and the speed of sound was assumed to be 340m/s. Further, the fully turbulent flow was assumed with free-stream level of turbulence of 2.6% and uniform inflow velocity distribution was set across the inflow boundary. The k-ω SST turbulence model was employed for all test cases, unless otherwise stated. The y+ parameter was estimated based on the flat-plate boundary layer theory. For given Reynolds number, inflow velocity $U_{\square}$, density ρ, dynamic viscosity μ and cord length c the y+ parameter was computed in the following steps:

1. Estimate skin friction coefficient from the Schlichting correlation:

$$C_f = [2 \cdot log_{10}(Re) - 0.65]^{-2.3} \tag{9}$$

2. Obtain wall shear stress from the definition of C_f:

$$\tau_w = C_f \cdot 0.5 \cdot \rho \cdot U_\infty^2 \tag{10}$$

3. Compute the friction velocity from the definition:

$$U_* = \sqrt{\tau_w / \rho} \tag{11}$$

4. Compute y+ parameter from the definition, where y is the employed spacing next to the wall:

$$y+= y \cdot \rho \cdot U_* / \mu \tag{12}$$

For the presented test cases with trailing and leading edge flaps, the inflow wind speed was set to 11.4m/s, and the rotational speed of the rotor was set to 9.6rpm

4.1 Numerical methods

The HMB2 code is a 3D multi-block structured solver for the 3D Navier-Stokes equations. HMB2 solves the Navier-Stokes equations in integral form using the arbitrary Lagrangian-Eulerian formulation for time-dependent domains with moving boundaries. The solver uses a cell-centred finite volume approach combined with an implicit dual-time method. [Osher1983]'s upwind scheme is used to resolve the convective fluxes, and MUSCL [VanLeer1979] variable extrapolation is used to provide formally third-order accuracy on uniform grids. Central differencing (CD) spatial discretisation is used for the viscous terms. The non-linear system of equations that is generated as a result of the linearization is solved by integration in pseudo-time using a first-order backward difference method based on [Jameson1991]'s pseudo-time integration approach. A Generalised Conjugate Gradient (GCG) method is then used [Eisenstat1983] in conjunction with a Block Incomplete Lower-Upper (BILU) factorisation as a

pre-conditioner. The HMB2 solver has a library of turbulence closures including several one- and two- equation models. Turbulence simulation is also possible using either the Large-Eddy or the Detached-Eddy simulation approach [Spalart1997]. The solver was designed with parallel execution in mind and the MPI library along with a load-balancing algorithm are used to this end. The flow solver can be used in serial or parallel fashion for large-scale problems. Depending on the purposes of the simulations, steady and unsteady wind turbine CFD simulations can be performed in HMB2 using single or full rotor meshes generated using the ICEM-Hexa tool. Rigid or elastic blades can be simulated using static or dynamic computations. HMB2 allows for sliding meshes to simulate rotor-tower interaction cases [Steijl2008]. Alternatively, overset grids can be used [Jarkowski2013]. To account for low-speed flows, the Low-Mach Roe scheme (LM-Roe) developed by [Rieper2011] is employed for wind turbine cases [Carrion2013].

The HMB2 CFD solver has so far been validated for several wind turbine cases, including the NREL Annex XX experiments [Gomez-Iradi2004], where the effect of the blades passing in front of the tower was captured. The pressure and PIV data of the MEXICO project [Carrion2014] have also been used for validation, where the wake was resolved on a fine mesh capable to capture and preserve the vortices downstream the rotor, which enabled the prediction of the onset of wake instabilities [Carrion2015].

A new flap deflection algorithm was implemented in HMB2 to allow arbitrary flap shape motion. The algorithm is based on the surface interpolation, where the mean, maximum and minimum flap deflection is defined by a separate surface. Then, the linear interpolation is employed for each point on the surface between the mean and deflected shape of the flap. The motion of the flap can be a complex function of time *i.e.* not a simple function like $sin(\omega t)$ or $cos(\omega t)$. In this case the motion is described by a Fourier series of arbitrary number of harmonics. It must be noted here, that since only mean and maximum surfaces are known to the solver, the interpolation tends to shrink the flap slightly. To understand this behaviour, consider a 2D rod-like flap shown in Figure 15. As can be seen, the linear interpolation tends to shrink the flap, but the effect is not pronounced for relatively small angles of deflection.

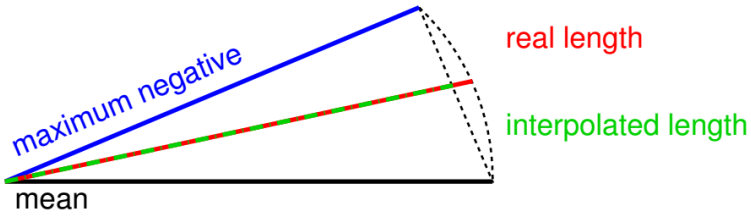

Figure 15: Schematic of the trailing edge flap, showing mean and maximum negative deflections, and real and interpolated length of the flap during motion.

4.2 Mesh convergence study

The mesh convergence study was performed before various test cases were computed to find the required density of the mesh and cell distribution in vicinity to the blade surface. Only 70% of the blade were modelled for this study – from 0.3R to 1R, where R is the radius of the blade. The flow around the blade was considered to be periodic in space and time. This allowed the use of the HMB2 “hover” formulation described in details in [Steijl2006]. The formulation includes a combination of mesh motion and additional source terms in the Navier-Stokes

equations. The spinner was approximated with a long cylinder running parallel to the flow along the computational domain. The free-stream was kept to the level of turbulence of 2.6%, and the k-ω turbulence model was employed. The conditions selected for the mesh convergence study are presented in Table 5. The domain size and boundaries are shown in Figure 16, and the results of the mesh convergence study are presented in Figure 17. This study showed that the mesh density between 3M to 5M cells per one blade is sufficient to obtain mesh independent solution.

U_{wind}	11m/s
U_{tip}	82.437m/s
RPM	8.836
Re_{tip}	$34.817 \cdot 10^6$
$M_{tip}=U_{tip}/U_{sound}$	0.243
λ	7.494
Pitch angle	0°

Table 5: Computational conditions for the mesh convergence study.

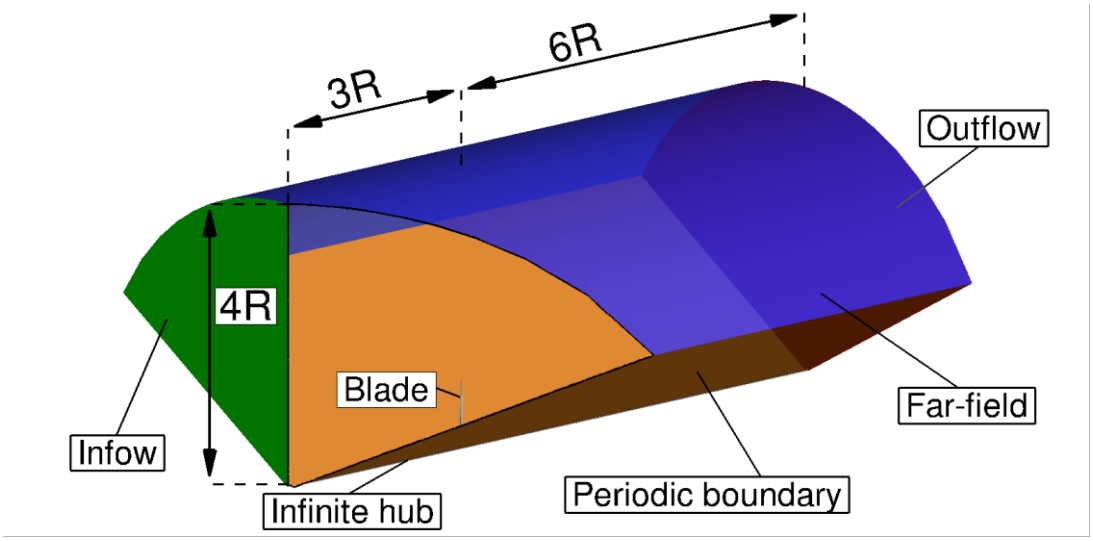

Figure 16: Computational domain for mesh convergence study with employed boundary conditions. Part of the domain removed to expose the blade

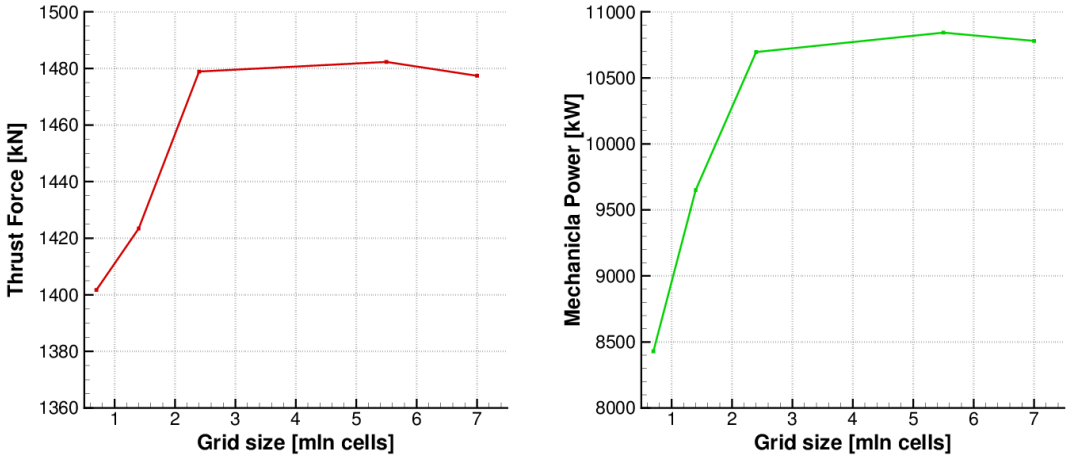

a) Thrust force b) Mechanical Power

Figure 17: Thrust fore and mechanical power as function of computational grid density.

4.3 Computational grid

Based on the mesh study, a fine mesh consisting of 9.2M points was constructed and included the necessary refinement to allow for the flaps deformation. The computational domain had the same dimensions as for the grid convergence study shown in Figure 16. The grid included the complete DTU 10MW RWT blade in a straight configuration, and possessed 0-grid topology around the aerofoil sections as shown in Figure 18a. The first cell distance from the wall was set to 10^{-6}c, where c=6.206m is a maximum chord of the blade. This allowed to estimate the y+ parameter for this girds at rated conditions based on the wind speed as y+=0.2. The blade was modelled in the straight configuration with simplified nacelle, as shown in Figure 19. The simplified nacelle shape was obtained by rotating the hub of the rotor by 180°.

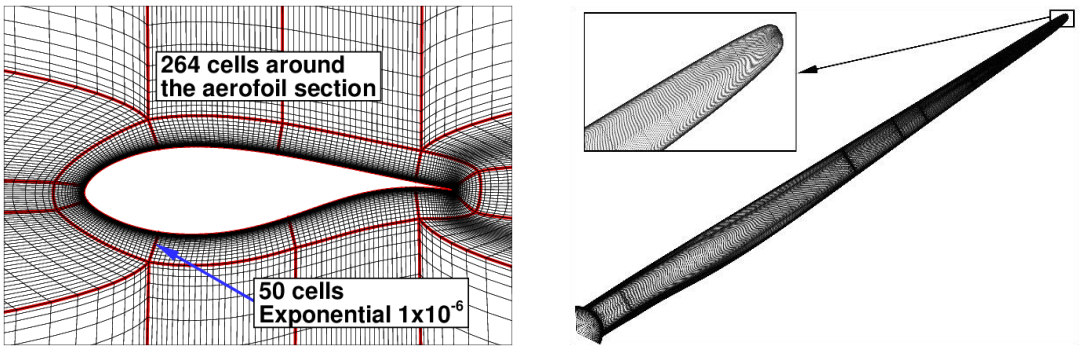

a) Slice through 9.2M mesh. b) Surface grid for 9.2M mesh.

Figure 18: Slices through mesh in vicinity to the surface of the blade (a); and surface grids (b) for 9.2M cells grid.

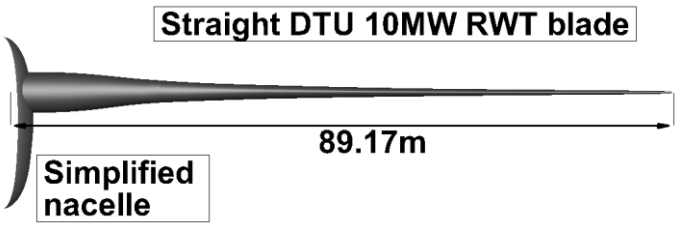

Figure 19: Shape of the DTU 10MW RWT blade with simplified nacelle as employed for the 9.2M cells mesh.

4.4 Definition of the flaps

The DTU 10-MW RWT blade was equipped with leading and trailing edge flaps. The leading edge (LE) flap was located at 60%R station, and the trailing edge (TE) flap was located at 75%R. The length of each flap was 10%R, but the width of the TE flap was 10% of the local chord, whereas the width of the LE flap was 20% of the local chord, as shown in Figure 20a. The choice of the TE flap width was made under the understanding that flaps will be used for load control and elevation. For the LE flap, it was assumed that its operation is similar but less efficient to that of the TE flap. The width in this case is increased to 20% so as to allow larger control surface and a smooth transition of the surface slope.

The deformation of the flaps was defined with respect to the mean line of the aerofoils as indicated in Figure 21. Let $\boldsymbol{X}_m$ denote the mean line and $h(x)$ denote the thickness distribution. With respect to a curvilinear (ξ, η) system following the mean line, the deformation can be defined as $\eta(\xi) = \alpha\xi^2(3-\xi)/2$, where $\xi \in [0,1]$, and α is providing the deflection. In principle $\alpha \equiv \alpha(t) = \alpha_m \sin(\omega t)$, where α_m is the maximum value which is determined by the maximum deflection angle β. Then the upper (+) and lower (-) sides of the aerofoil are:

$$(\pm) = \boldsymbol{X}_m + \eta(\xi)\boldsymbol{N}_m + h(x)\boldsymbol{N'}_m \tag{13}$$

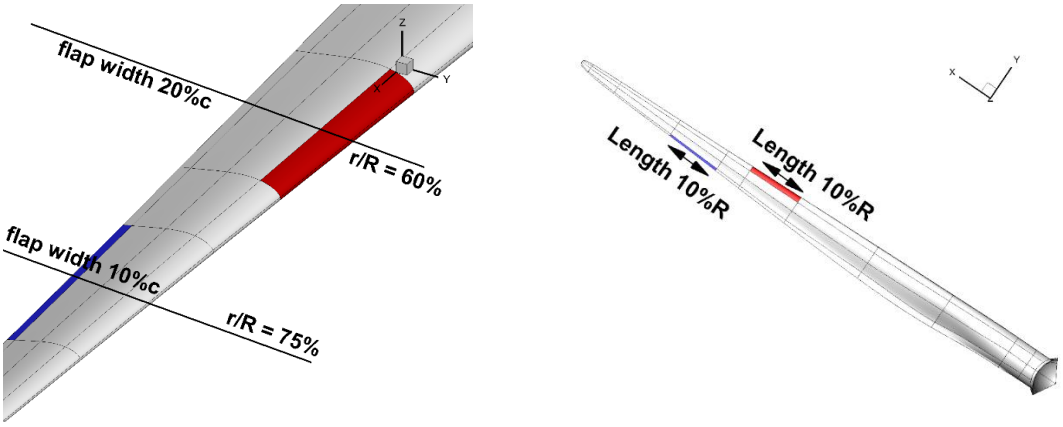

a) Location and width of the flaps. b) Length of the flaps.

Figure 20: The location and dimensions of the trailing and leading edge flaps.

In the above expression $\boldsymbol{N}_m$ denotes the unit normal to the mean line, and $\boldsymbol{N'}_m$ denotes the unit normal to the deformed mean line defined by $\boldsymbol{X'}_m = \boldsymbol{X}_m + \eta(\xi)\boldsymbol{N}_m$. By denoting the point at which the flap starts with x_0, the process to compute flap deflection is as follows:

For each point $x > x_0$

1. Get $\boldsymbol{X}_m(x)$, $h(x)$ and $\boldsymbol{N}_m(x)$
2. Define $\xi = \xi(x)$ based on the length along the mean line
3. Define the deformed mean line $\boldsymbol{X'}_m(\xi) = \boldsymbol{X}_m(x) + \eta(\xi)\boldsymbol{N}_m(x)$ and get $\boldsymbol{N'}_m(\xi)$
4. Compute $\boldsymbol{X}(\pm) = \boldsymbol{X}_m + \eta(\xi)\boldsymbol{N}_m + h(x)\boldsymbol{N'}_m$

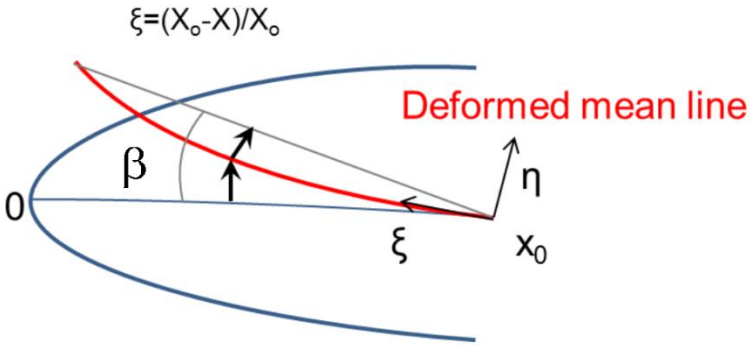

a) Definition for the LE flap deformation.

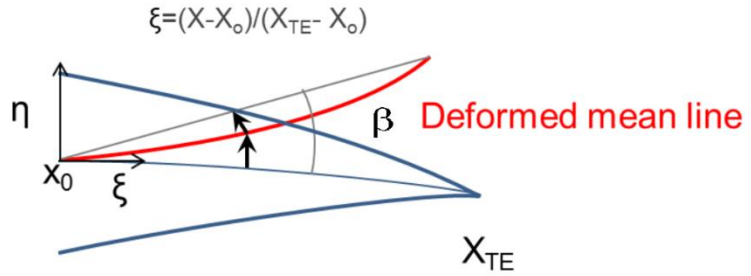

b) Definition for the TE flap deformation.

Figure 21: Definition conditions for the LE (a) and TE (b) flap deformation.

The FORTRAN code to compute the deflection of the TE and LE flaps is presented in Appendix A. The flaps were deflected form -10° to 10° with the shape and notation presented in Figure 22. The frequency of flap motion was set to 0.96Hz, or six times per revolution.

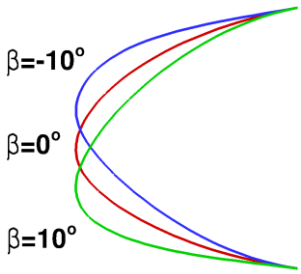

a) Deflection of the LE flap.

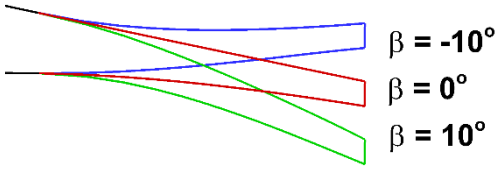

b) Deflection of the TE flap.

Figure 22: Definition of the positive and negative deflection fot the LE (a) and TE (b) flap.

4.5 Results for the TE flap

The results for the DTU 10-MW reference wind turbine equipped with the trailing edge flap in form of span-wise load distributions are shown in Figure 23. Flap oscillates at frequency 0.96Hz – six times per revolution. The length of each section in radial direction used in pressure integration is $\Delta r = 2.15m$.

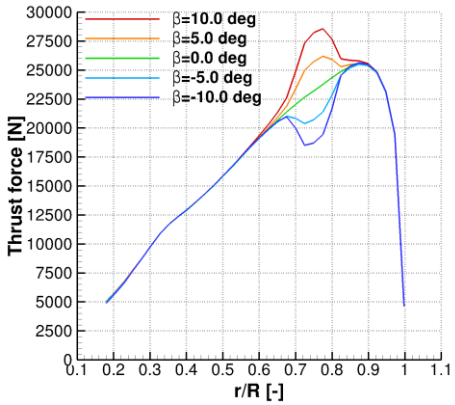

a) Distribution of thrust force.

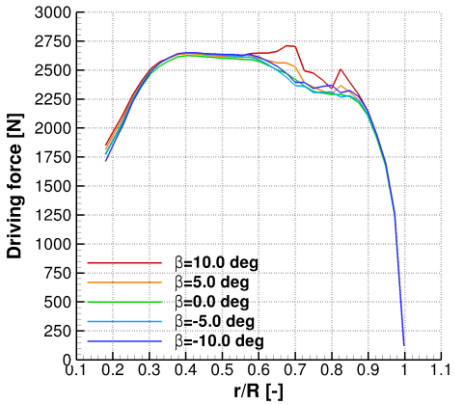

b) Distribution of driving force.

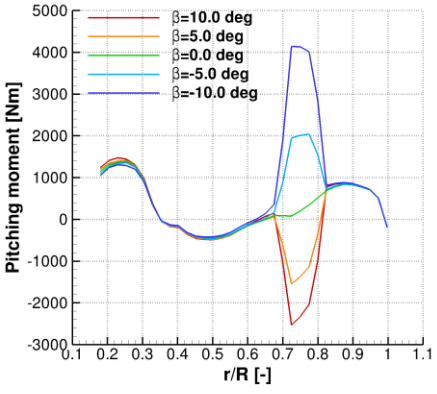

c) Distribution of pitching moment.

Figure 23: Span-wise distribution of thrust force (a), driving force (b) and pitching moment (c) for DTU blade equipped with TE flap. Flap motion frequency f=0.96Hz (6 times per revolutuon).

4.6 Results for the LE flap

The results for the DTU 10-MW reference wind turbine equipped with the leading edge flap in form of span-wise load distributions are shown in Figure 24. Flap oscillates at frequency 0.96Hz – six times per revolution. The length of each section in radial direction used in pressure integration is $\Delta r = 2.15m$.

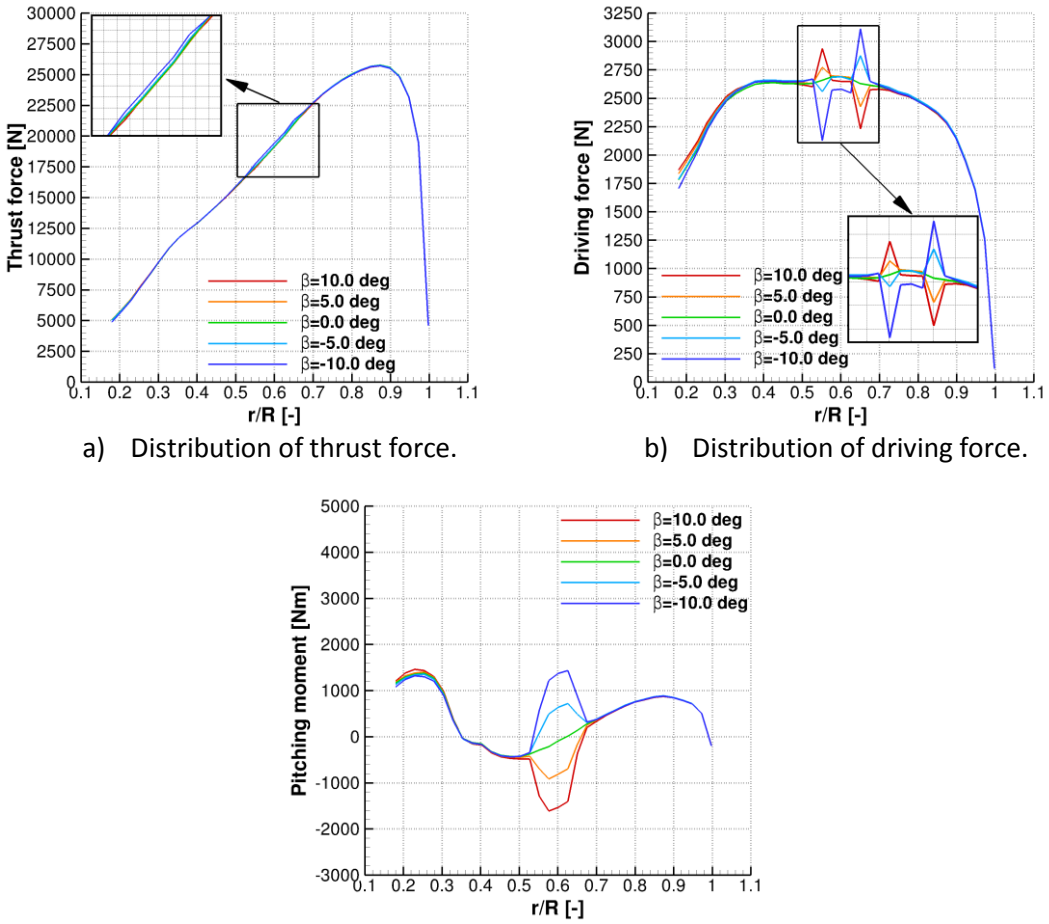

a) Distribution of thrust force.

b) Distribution of driving force.

c) Distribution of pitching moment.

Figure 24: Span-wise distribution of thrust force (a), driving force (b) and pitching moment (c) for DTU blade equipped with LE flap. Flap motion frequency f=0.96Hz (6 times per revolutuon).

4.7 Comparison of the performance

In order to conduct a meaningful comparison of the performance of both flaps the non-dimensional coefficients were used. This was chosen, since flaps are located at different radial position and exhibit different inflow conditions. For this, the normal force coefficient (CN), tangential force coefficient (CT) and pitching moment coefficient (CM) were computed. First, the

thrust and driving forces were projected on the normal and tangential directions using local geometrical pitch angle *α* as:

$$F_N = T_F \cdot \cos(\alpha) + D_F \cdot \sin(\alpha) \tag{14}$$

$$F_T = D_F \cdot cos(\alpha) - T_F \cdot sin(\alpha) \tag{15}$$

The thrust force T_F and driving force D_F are defined in Figure 25, and were obtained from the surface pressure integration in the middle of the flap with the length of the section in radial direction $\Delta r = 2.15m$. Note, that the geometrical pitch angle *α* is defined in [Bak2015], and is constant *i.e.* it does not change with the flap angle *β*. Then, the forces and moment were non-dimensionalised as:

$$CN = \frac{F_N}{0.5\rho U^2 A} \tag{16}$$

$$CT = \frac{F_T}{0.5\rho U^2 A} \tag{17}$$

$$CM = \frac{M_P}{0.5\rho U^2 Ac} \tag{18}$$

where *U* and *A* are the geometrical local inflow velocity and the local platform area, respectively. The inflow velocity is defined as:

$$U^2 = (\Omega r)^2 + U_{wind}^2 \tag{19}$$

and the platform area is defined as:

$$A = \Delta r \cdot c \tag{20}$$

where *c* is the local chord in the middle of the flap.

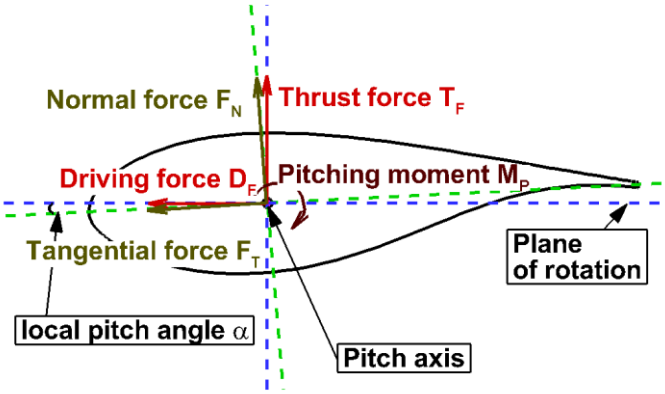

Figure 25: Definition of the normal force, tangential force and pitching moment. Quantities shown in the directions defined as positive.

Obtained coefficients for both flaps as function of the flap angle *β* are compared in Figure 26. As can be seen, the trailing edge flap significantly modifies all three non-dimensional coefficients. On the other hand, leading edge flap has the most pronounced effect on the pitching moment coefficient, and almost negligible (as compared to the TE flap) influence on the normal force

coefficient. Further, the relative change and slope of the pitching moment coefficient is higher for the trailing edge flap. Finally, both flaps can change the tangential force coefficient, but the TE flap has higher hysteresis loop, as compared to the results for the LE flap.

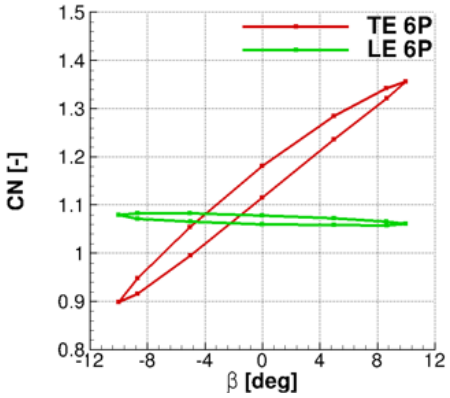

a) Normal force coefficient.

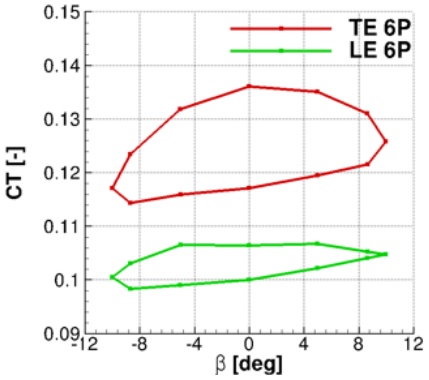

b) Tangential force coefficient.

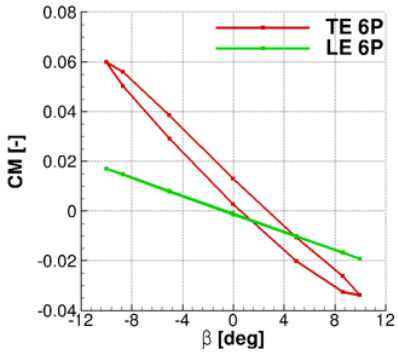

c) Pitching moment coefficient.

Figure 26: Comparison of the performance of TE and LE flaps based on the non-dimentsional coeffcients as function of flap deflection angle.

4.8 Summary

The results showed significant, but localized effect of the flap deflection on the distribution of the loads. The trailing edge flap can modify both thrust force and pitching moment, whereas trailing edge flap mostly affects the pitching moment. That suggests, that trailing edge flap can be used to locally change aerodynamic loads on the blades, possibly eliminating the adverse effect of the blade passing in front of the tower. On the other hand the leading edge flap can be used to counter the additional pitching moment created by the deflection of the trailing edge flap.

4.9 CFD analysis of large off-shore wind turbines: *Published Work*

- V. Leble, G. Barakos – “Detailed Simulation of Offshore Wind Turbine”, under review at Journal of Fluids and Structures
- V. Leble, G. Barakos, “Static and dynamic aeroelastic calculations for 10-MW wind turbines”, MARE-WINT side event, EWEA Offshore 2015, Copenhagen, Denmark, March 2015

- V. Leble, G. Barakos, “Dynamic analysis of Off-Shore Wind Turbines”, poster presentation at EPSRC Supergen Wind Hub General Assembly, April 2015, Loughborough, UK
- V. Leble, G. Barakos – “Coupled NS/SPH Analysis of Off-Shore Wind Turbine”, In proceedings of 71st American Helicopter Society Annual Forum & Technology Display, Virginia Beach, VA USA, May 2015
- V. Leble, Y. Wang, G. Barakos, “CFD analysis of 10-MW wind turbines”, In proceedings of DEWEK 2015, Bremen, Germany, May 2015
- Y. Wang, V. Leble, M. White, G. Barakos, “Wake Characteristics of Large-scale Wind Turbines”, In proceedings of 2015 European Rotorcraft Forum, Munich, Germany, September 2015
- V. Leble, Y. Wang, G. Barakos, “Detailed Simulation of Offshore Wind Turbine”, accepted for oral presentation at EWEA Conference 2015, Paris, France, November 2015

References

[Bak2013] Bak C, Zahle F, Bitsche R, Kim T, Yde A, Henriksen L C, Natarajan A and Hansen M H (2013) Description of the DTU 10 MW reference wind turbine, *DTU Wind Energy Report-I-0092*

[Braga2014] Braga DFO, Tavares SMO, da Silva LFM, Moreira PMGP and de Castro PMST (2014): Advanced design for light-weight structures: review and prospects, Progr. Aerospace Sci. 69, 29-39. (doi:10.1016/j.paerosci.2014.03.003)

[Carrion2013] Carrión M, Woodgate M, Steijl R, Barakos G. (2013): Implementation of all-mach roe-type schemes in fully implicit CFD solvers – demonstration for wind turbine flows. International Journal for Numerical Methods in Fluids 2013; 73(8):693–728 (doi:10.1002/fld.3818)

[Carrion2014] Carrión M, Steijl R, Woodgate M, Barakos G, Munduate X, Gomez-Iradi S. (2014): Computational fluid dynamics analysis of the wake behind the MEXICO rotor in axial flow conditions. Wind Energy 2014 (doi:10.1002/we.1745)

[Carrion2015] Carrión M, Woodgate M, Steijl R, Barakos GN, Gomez-Iradi S, Munduate X. (2015): Understanding wind-turbine wake breakdown using computational fluid dynamics. AIAA Journal 2015; 53(3):588 – 602 (doi:10.2514/1.J053196)

[Eisenstat1983] Eisenstat SC, Elman HC, Schultz MH. (1983): Variational iterative methods for nonsymmetric systems of linear equations. SIAM Journal on Numerical Analysis 1983; 20(2):345–357, (doi:10.1137/0720023)

[Gilmar2015-DAMAS] Pereira G, Mikkelsen L.P, McGugan M, Embedded Fibre Bragg Grating Sensor Response Model: Crack Growing Detection in Fibre Reinforced Plastic Materials, 2015 Journal of Physics: Conference Series, 628,012115, (doi:10.1088/1742-6596/628/1/012115)

[Gomez-Iradi2009] Gómez-Iradi S, Steijl R, Barakos GN. (2009): Development and validation of a CFD technique for the aerodynamic analysis of HAWT. Journal of Solar Energy Engineering 2009; 131(3):031 009 (doi:10.1115/1.3139144)

[Hill1997] Hill KO, Meltz G. Fiber Bragg grating technology fundamentals and overview. Journal of Lightwave Technology. 1997;15(8):1263-1276.

[Jameson1991] Jameson A. (1991): Time Dependent Calculations Using Multigrid, with Applications to Unsteady Flows Past Airfoils and Wings, 10th Computational Fluid Dynamics Conference, Honolulu, HI, 24-26 June 1991, AIAA-1991-1596.

[Jarkowski2013] Jarkowski M, Woodgate MA, Barakos GN, Rokicki J. (2013): Towards consistent hybrid overset mesh methods for rotorcraft CFD. International Journal for Numerical Methods in Fluids 2013; 74(8):543–576 (doi:10.1002/fld.3861)

[Jülich2010] Jülich, F. and Roths, J. (2010): Comparison of transverse load sensitivities of fibre Bragg gratings in different types of optical fibres. 7726(0):77261N–77261N–9.

[Magne1997] S. Magne, S. Rougeault, M. Vilela, P. Ferdinand, State-of-strain evaluation with fiber Bragg grating rosettes: application to discrimination between strain and temperature effects in fiber sensors., Applied Optics 36 (36) (1997) 9437–9447. (doi:10.1364/AO.36.009437)

[McGugan2015] McGugan M, Pereira G, S_rensen BF, Toftegaard H, Branner K. Damage tolerance and structural monitoring for wind turbine blades. Philosophical Transactions of the Royal Society of London A: Mathematical, Physical and Engineering Sciences. 2015;373(2035).

[Osher1983] Osher S, Chakravarthy S. (1983): Upwind schemes and boundary conditions with applications to Euler equations in general geometries. Journal of Computational Physics June 1983; 50(3):447–481.

[Peters] Peters, K., Studer, M., Botsis, J., Iocco, A., Limberger, H., and Salath, R. Embedded Optical Fiber Bragg Grating Sensor in a Nonuniform Strain Field : Measurements and Simulations. pages 19–28.

[Peters2001] Peters K, Studer M, Botsis J, Iocco A, Limberger H, Salath R. Embedded Optical Fiber Bragg Grating Sensor in a Nonuniform Strain Field: Measurements and Simulations. Experimental Mechanics. 2001;41(1):19-28.

[Rieper2011] Rieper F. (2011): A low-mach number fix for roe's approximate riemann solver. J. Comput. Phys. Jun 2011; 230(13): 5263–5287 (doi:10.1016/j.jcp.2011.03.025)

[Spalart1997] Spalart PR, Jou W, Strelets M, Allmaras SR. (1997): Comments on the Feasibility of LES for Wings, and on a Hybrid RANS/LES Approach. Proceedings of the First AFOSR International Conference on DNS/LES, 1997

[Stejl2006] Steijl R., Barakos G., and Badcock K. (2006): A framework for CFD analysis of helicopter rotors in hover and forward flight. International Journal for Numerical Methods in Fluids, Volume 51, Issue 8, pages 819–847, 20 July 2006 (doi: 10.1002/fld.1086)

[Steijl2008] Steijl R, Barakos G. (2008): Sliding mesh algorithm for CFD analysis of helicopter rotor-fuselage aerodynamics. International Journal for Numerical Methods in Fluids 2008; 58(5):527–549 (doi:10.1002/fld.1757)

[SørensenL2007]Sørensen, L., Botsis, J., Gmür, T., and Cugnoni, J. (2007): Delamination detection and characterisation of bridging tractions using long FBG optical sensors. Composites Part A: Applied Science and Manufacturing, 38(10):2087–2096.

[SørensenBF2010] Sørensen (2010): Technical Univ. of Denmark, R. N. L. f. S. E. M. R. D. Cohesive laws for assessment of materials failure: Theory, experimental methods and application. Risø DTU.

[VanLeer1979] Van Leer B. (1979): Towards the Ultimate Conservative Difference Scheme, V. A Second Order Sequel to Godunovs Method, J. Comp. Phys. 32 (1979), 101-136

Appendix A

A.1. FORTRAN code to compute the trailing and leading edge flap deflections

```
! Let X(i), Y(i) denote the coordinates of the nodes on the aerofoil
! Input: Xo (x/c location), amax (max angle), freq (frequency)
! Function: f(x,t)=amax*sin(2.*pi*freq*t)*ksi**2*(3.-ksi)/2.
! N number of points on the aerofoil
! Note: all dimensions are normalized to the chord
! TE Flap motion:
do i=1,N
   Ynew=Y(i); dYnew=0.
   If(X(i).ge.Xo) then
              ksi=(X(i)-Xo)/(XTE-Xo) ! XTE=1.
              dmax=(XTE-Xo)*sin(amax)/cos(amax)
              Ynew=Y(i)+ dmax*sin(2.*pi*freq*t)*ksi**2*(3.-ksi)/2.
              dYnew= 2*pi*freq*dmax*cos(2.*pi*freq*t)*ksi**2*(3.-ksi)/2.
   endif
enddo
! LE Flap motion:
do i=1,N
   Ynew=Y(i); dYnew=0.
   If(X(i).le.Xo) then
              Ksi=(Xo-X(i))/Xo
              dmax=Xo*sin(amax)/cos(amax)
              Ynew=Y(i)+ dmax*sin(2.*pi*freq*t)*ksi**2*(3.-ksi)/2.
              dYnew= 2*pi*freq*dmax*cos(2.*pi*freq*t)*ksi**2*(3.-ksi)/2.
   endif
enddo
```

Acknowledgements

George Barakos, Professor (Aerospace Sciences), University of Glasgow
Supervisor for Vladimir Leble's work

Bent F. Sørensen, Head of Section (Composite materials and Mechanics), DTU Wind Energy
Co-supervisor for Gilmar Pereira's work

Lars P. Mikkelsen, Associate Professor, DTU Wind Energy
Co-supervisor for Gilmar Pereira's work

DTU Wind Energy is an institute of the Technical University of Denmark featuring a unique integration of research, education, innovation and public / private consultancy in wind energy. Our activities contribute to new opportunities and technologies for the exploitation of wind energy, both globally and nationally. The research focuses on specific technical and scientific areas that are central to the development, innovation and use of wind energy, and is the basis for high quality education at the university.

We have more than 240 employees of which around 60 are Ph.D. students. Research is carried out within nine research programs organised into three main groups: wind energy systems, wind turbine technology and the basis for wind energy.

Danmarks Tekniske Universitet
DTU Vindenergi
Nils Koppels Allé
Bygning 403
2800 Kgs. Lyngby
Telefon 45 25 25 25

info@vindenergi.dtu.dk
www.vindenergi.dtu.dk